



Nonlinear effects of the biosynthesis temperature of ZnO nanoparticles on their structural, optical, and ultraviolet blocking parameters

Mohyelddine Alqubati^{1,2} · Samir Osman Mohammed Osman^{2,3} · Mansour S. Abul Galil^{4,5} · Mohamed Ali Algradee^{3,6} · A. Mohammed Sultan³ · Abdullah M. Qaid^{3,6}

Received: 20 August 2023 / Accepted: 27 August 2023 / Published online: 22 September 2023
© The Author(s), under exclusive licence to The Optical Society of India 2023

Abstract The surge in the incidence of skin cancer caused by UV exposure in Yemen served as the impetus for the current study. Fixed volumes and concentrations of both propolis aqueous extract and zinc salt solution were reacted to form zinc oxide (ZnO) nanoparticles at various temperatures (25, 35, 50, 65, 75, and 90 °C) and at a constant pH. The characteristics of the nanostructure and the degree of deformation that took place inside the nanoparticles were determined (for example, microstrain, stacking fault, surface stress, porosity, etc.). The optical parameters that affect the estimation of the blocking ultraviolet radiation parameters, such as the absorption coefficient, extinction coefficient, skin depth, refractive index, energy gap, Urbach energy, and optical conductivity, were calculated. The best results obtained in blocking ultraviolet radiation (A and B) were 81% and 75% for the sample that was prepared at 75 °C, respectively. Based on scientific methodology, empirical data, and exact equations, the results were interpreted within the nanoscale structure.

Keywords ZnO · Propolis · UV-blocking · Optical · Optical activity · Refractive index

Introduction

Many environmental studies on climate change confirm the direct incremental relationship between wars and global warming, and this is what makes the matter worse in Yemen with the existing humanitarian crisis and the continuation of the war [1–3].

Climate change in Yemen in recent years has led to a lack of rain and an increase in temperatures [3, 4], and the exposure of the displaced and those fleeing from the war [5, 6], whose numbers are increasing as the war continues, to ultraviolet rays due to their loss of what shields their bodies from the sun, such as their homes or clothes. Surveys show that the number of cases of skin cancer in hot areas in Yemen has increased in the recent period, especially in children and young adults [7, 8].

The intense energy and short wavelength of ultraviolet (UV) rays, which range from 200 to 400 nm, allow them to penetrate the human body and seriously harm health, such as causing cataracts, skin cancer, and weakened immune systems [9–11]. The synthesis and development of materials that lower the risks associated with ultraviolet radiation have been highlighted as one of the most significant industrial and medical applications of nanotechnology. Many studies on the ability of nanoparticles to block this radiation and reduce its damage have yielded scientific solutions [12–14].

The majority of scientific studies have linked the morphological and optical properties of nanoparticles to their capacity for blocking and absorbing UV radiation. In all these published articles, the most important structural parameters of the nanoparticles, which affect their ability to

✉ Samir Osman Mohammed Osman
samir.qa@just.edu.ye; samirbas@gmail.com

¹ Physics Department, Faculty of Applied Science, Taiz University, Taiz, Yemen

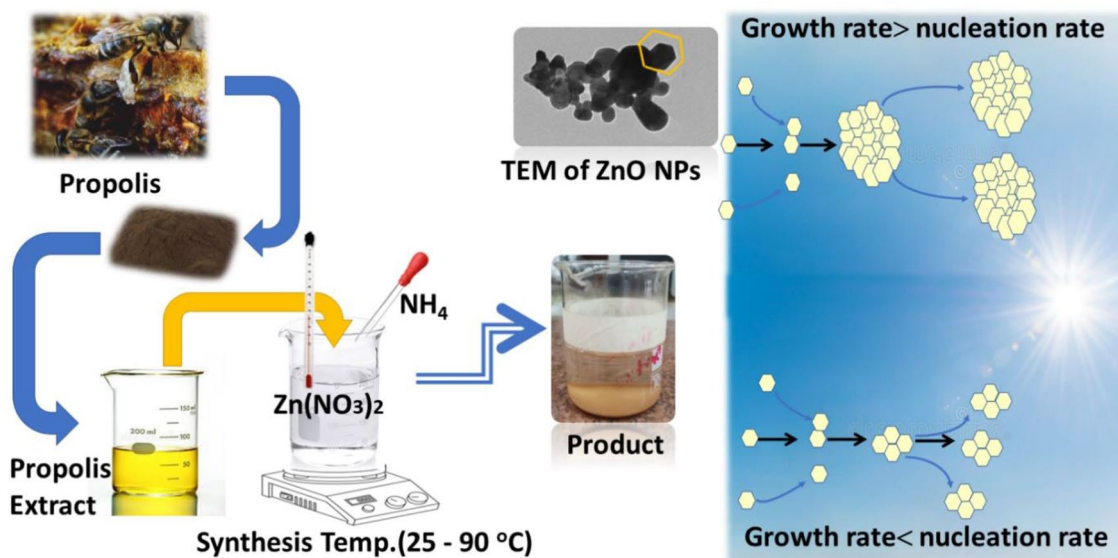
² Faculty of Engineering, Al-Janad University for Science and Technology, Taiz, Yemen

³ Physics Department, Faculty of Science, Ibb University, Ibb, Yemen

⁴ Chemistry Department, Faculty of Applied Science, Taiz University, Taiz, Yemen

⁵ Faculty of Medical Science, Al-Janad University for Science and Technology, Taiz, Yemen

⁶ Faculty of Science and Engineering, Aljazeera University, Ibb, Yemen



Scheme 1 A graphic abstract of the work

shield radiation, were computed. Through countless in-depth scientific calculations and studies over the past few years, it has been proven that green-manufactured zinc oxide nanoparticles are more effective in blocking and absorbing UV rays [15–18]. Therefore, these nanoparticles have been used in industrial and medical applications, for example, energy storage devices, optoelectronic devices, gas sensors, and other uses in the field of environmental remediation [19–21].

On the other hand, the latest survey for many applications and research on propolis, which is one of the products of honey bees, gave positive results about its ability to block ultraviolet rays due to its chemical composition and containment of many effective groups, which play a prominent role in blocking ultraviolet rays [22–24].

The hypothesis of this work was based on the fact that increasing the reaction temperature (during the formation of nanoparticles) will affect the optical properties (such as energy gap and optical activity) and also the unit cell parameters of zinc oxide nanocrystals without regard to the annealing temperature, as mentioned in some research [25, 26]. Most studies have shown the effect of annealing temperature on these properties [27–31], and therefore this research is considered somewhat different from these works because it studies the effect of biosynthesis temperature (in a wide range from 25 to 90) with the presence of propolis on these parameters.

In this current research, an attempt was made to study the effect of the biosynthesis temperature on the morphological structure, the optical properties of the biosynthesis of zinc oxide nanoparticles using propolis, and the ability of these particles to block ultraviolet rays. This research builds

on a previous study that used propolis to optimize the biosynthesis of zinc oxide nanoparticles [32].

The novel finding is the nonlinear relationship between the biosynthesis temperature of ZnO nanoparticles and their structural, optical, and UV-blocking parameters. As well, the importance of this work lies in the possibility of controlling the properties of zinc oxide through selecting the optimum temperature in the crystallization reaction; in other words, the emergence of the property of selectivity in temperature. (Scheme 1)

Materials and methods

Materials and chemicals

The propolis was purchased at the market. Deionized water (DI) was used throughout. Loba Chemie, an Indian company, provided the $\text{Zn}(\text{NO}_3)_2 \cdot 6\text{H}_2\text{O}$. Merck (Darmstadt, Germany) supplied the ammonia and ethanol.

Propolis aqueous extract preparation

In our previous work, we already described how to prepare an aqueous extract of propolis [33]. In general, 50 mL of DI water was mixed with 0.25 g of fine propolis powder and heated to 60 °C for half an hour with magnetic stirring. The mixture was then allowed to cool in the air before being filtered with filter paper to get rid of any solid impurities. The resultant solution, a yellowish-brown solution, was kept for use in the investigation's later steps.

The green synthesis of ZnO nanoparticles

This synthesis was described in detail in our previous work [32]. Six samples were prepared by combining 60 mL of 0.202 M $\text{Zn}(\text{NO}_3)_2 \cdot 6\text{H}_2\text{O}$ with 20 mL of propolis aqueous extract to investigate the effect of temperature on the biogenesis of ZnO nanoparticles. The pH was 8 for all the prepared samples. The samples were cooked for the same period of time (1 h), but at various temperatures (25, 35, 50, 65, 75, and 90 °C) and labeled PZ1, PZ2, PZ3, PZ4, PZ5, and PZ6, respectively. By using UV–Vis absorption and X-ray diffraction, respectively, ZnO nanoparticle production was confirmed.

Characterization techniques of ZnO nanoparticles

Several pertinent strategies and techniques were used to examine the structure and properties of ZnO nanoparticles.

The UV–Vis absorbance of the prepared samples of ZnO nanoparticles was measured by a Shimadzu Ultraviolet Spectrometer 2700. A Lumina fluorescence spectrometer (Thermo Fisher Scientific) was used for recording the photoluminescence (PL) spectra.

Using a PANalytical X'Pert Pro diffractometer equipped with a Cu target (operating conditions: 45 kV, 30 mA, line focus) and an X-ray source with a wavelength of 1.5406 nm, the temperature's effect on the biogenesis of ZnO nanoparticles was identified. The PEAKFIT and CHEKCELL software were employed to explore the crystal structure parameters of ZnO nanoparticles [34, 35].

The size and shape of the biosynthesised ZnO nanoparticles (50 °C) were studied using a JEOL GEM-1010 transmission electron microscope (TEM) with a 70-kV

accelerating voltage. A drop of the particle-containing solution was placed on a copper grid, and the water was allowed to evaporate at room temperature to dry the drop.

Results and discussion

Our current study will not explore the mechanism of zinc nanoparticle creation using the green technique because it was thoroughly covered in our earlier work [32]. The discussion will be focused on how to describe the relationship between the biosynthesis temperature and the morphological structure as well as the optical properties of these nanoparticles. Then, understanding the effect of these parameters and properties on the UV-blocking and UPF parameters for ZnO nanoparticles was attempted.

X-ray diffraction analysis and ZnO nanoparticle's structural parameters

The results of X-ray diffraction on prepared samples at various temperatures revealed peaks indicating crystallization areas in these samples. From Fig. 1, the peaks were almost at the following X-ray angles: 31.84°, 34.50°, 36.33°, 47.62°, 56.67°, 62.92°, 66.48°, 68.03°, and 69.17°. These sites are compatible with the following crystalline planes: (100), (002), (101), (102), (110), (103), (200), (112), and (201) [32]. These findings support previous findings that confirm the formation of the hexagonal zinc nanocrystals.

In Fig. 1a and b, it is possible to see the effect of the biosynthesis temperature by looking at the peaks in the XRD patterns of these samples. More clearly, some of the observed shifts in peak positions can be attributed to the

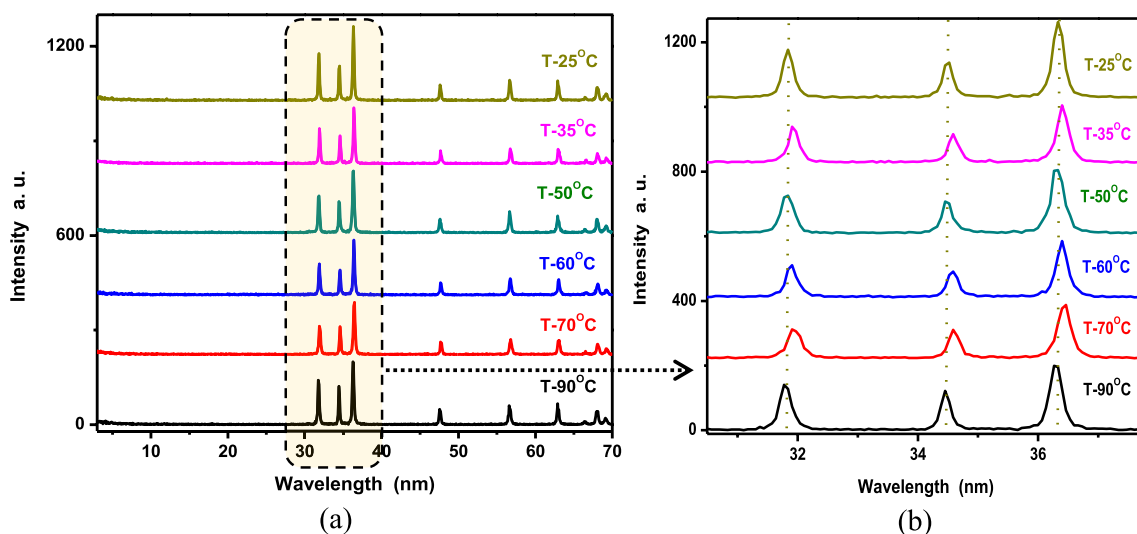


Fig. 1 a XRD patterns of the prepared samples. b The peak shifts of the XRD patterns of the prepared samples

biosynthesis temperature as a result of deformation in the ZnO nanocrystals, which can be represented as a change in the length of the bond between zinc and oxygen [36, 37].

To express the distortion in the zinc oxide nanocrystal, the interplanar distance d_{hkl} between the crystalline planes where the atoms are arranged was calculated using the diffraction angle values for all prepared samples, and the results were compared with standard JCPDS card No. 80-0075 [38] as shown in Table 1. The peak position shifts are noticeable, and the results are rather similar to the values of the reference standard.

Also, the apparent change in the values of d_{hkl} in the zinc oxide nanocrystals is related to the deformation of the bond length (Zn–O) [39]. For this purpose, a computer program (CHEKCELL) was used to determine these parameters by taking advantage of the values of the standard parameters (JCPDS card No. 80-0075, $a=0.3253$ nm, and $c=0.5206$ nm) [38] as initial inputs into the program, and the calculated results are written in Table 2. The bond length (Zn–O) was computed as follows:

$$L(Zn - O) = \sqrt{\frac{a^2}{3} + \left(\frac{1}{2} - u\right)^2 c^2}, \tag{1}$$

where a and c are unit cell parameters, while the parameter u is computed using the following equation:

$$u = \frac{a^2}{3c^2} + 0.25 \tag{2}$$

It is clear from Tables 1 and 2 that the presence of propolis during biosynthesis affected the crystalline growth of ZnO nanocrystals due to the capping of these nanoparticles with different sizes at every temperature. The kinetics and reaction rate of the biosynthesis of ZnO nanocrystals were sped up by the temperature increase from 25 to 90 °C. The temperature vs. unit cell volume relationship is nonlinear because the temperature effect depends on different factors,

Table 2 Unit cell parameters and Zn–O bond length of the prepared samples

Temperature (°C)	a (Å)	c (Å)	Volume (Å) ³	Zn–O bond length (Å)
25	3.246	5.200	47.450	1.8845
35	3.245	5.193	47.352	1.8831
50	3.248	5.202	47.514	1.8853
65	3.244	5.189	47.278	1.8821
75	3.241	5.193	47.248	1.8818
90	3.247	5.199	47.477	1.8848

such as zinc salt concentration, crystallization duration, the extracted solution quantity, and pH [40, 41]. It is worth noting that the formation mechanism of ZnO nanocrystals in our current research depends on the speed ratio between nucleation and growth processes, which is unstable for each temperature. That explains the nonlinear relationship between temperature and crystal size, or unit cell volume [42], which in turn leads to the emergence of heterogeneity of the nanocrystal, leading to the so-called deformation [43]. The process of crystal deformation can be demonstrated with a change in sample preparation temperature by drawing a relationship between the temperature of the samples and the c/a ratio in the unit cell and the length of the bond between zinc and oxygen, as in Fig. 2a.

The nonlinear relationship between temperature and crystal size reflects on the lattice parameters (a and c), as shown in Fig. 2b. From Fig. 2a, it is apparent that the change in the Zn–O bond as in sample PZ5 is uncoincidental with the change in the c/a ratio with temperature, and this further proves the incompatibility between nucleation and growth processes for ZnO nanocrystals [40].

In the following investigations, the structural parameters were calculated for the biosynthesized ZnO nanocrystal samples using the three permanent peaks of XRD

Table 1 hkl planes, d_{hkl} spacing, and 2θ parameters of the Standard JCPDS card No. 80-0075 and the ZnO nanoparticles samples

Standard JCPDS card No. 80-0075			T-25		T-35		T-50		T-65		T-75		T-90	
hkl	d_{hkl} nm	2θ deg	d_{hkl} nm	2θ deg	d_{hkl} nm	2θ deg	d_{hkl} nm	2θ deg	d_{hkl} nm	2θ deg	d_{hkl} nm	2θ deg	d_{hkl} nm	2θ deg
1 0 0	2.818	31.729	2.808	31.839	2.809	31.906	2.809	31.839	2.812	31.906	2.807	31.906	2.812	31.772
0 0 2	2.605	34.401	2.598	34.522	2.599	34.589	2.599	34.455	2.599	34.589	2.597	34.589	2.601	34.455
1 0 1	2.479	36.213	2.471	36.332	2.472	36.399	2.472	36.332	2.473	36.399	2.469	36.467	2.474	36.265
1 0 2	1.913	47.495	1.908	47.600	1.909	47.667	1.909	47.599	1.909	47.667	1.907	47.667	1.909	47.533
1 1 0	1.627	56.521	1.623	56.654	1.624	56.721	1.623	56.654	1.624	56.721	1.623	56.788	1.624	56.587
1 0 3	1.478	62.804	1.476	62.891	1.477	62.958	1.476	62.891	1.476	63.025	1.475	63.092	1.476	62.891
2 0 0	1.409	66.287	1.405	66.445	1.405	66.646	1.406	66.378	1.406	66.513	1.406	66.513	1.404	66.378
1 1 2	1.379	67.867	1.377	68.055	1.378	68.055	1.377	67.988	1.377	68.122	1.377	68.055	1.378	68.122
2 0 1	1.360	68.993	1.357	69.195	1.358	69.195	1.358	69.195	1.358	69.128	1.356	69.195	1.357	69.128

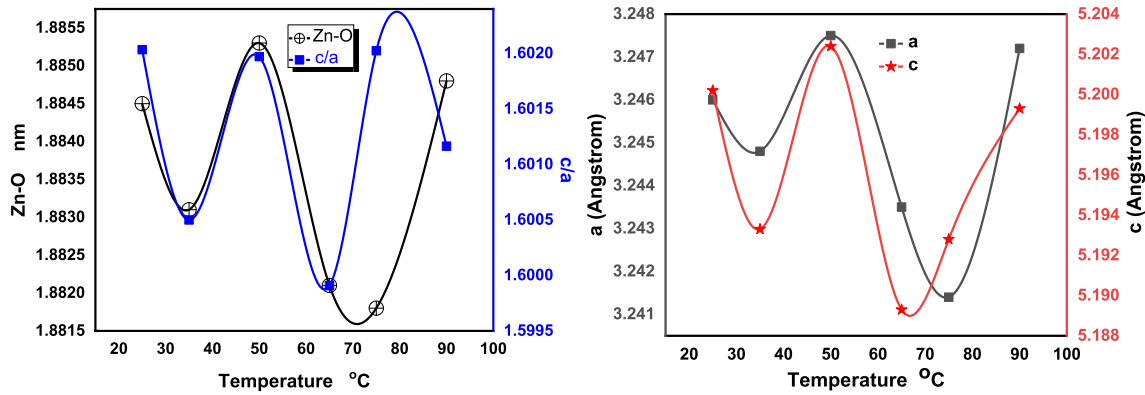


Fig. 2 a Bond length (Zn–O) & c/a ratio vs. temperature. b Lattice parameters (a & c) vs. temperature for the prepared samples

measurements. PEAKFIT was employed to refine and estimate the full-width-half-maximum (FWHM) of the XRD patterns’ peaks. The crystal size *D* and microstrain ϵ in the ZnO nanostructure were calculated using the Williamson–Hall method [44] and the equation:

$$FWHM_{(rad)} = \frac{k\lambda}{D \cos \theta} + 4\epsilon \tan \theta, \tag{3}$$

where $k=0.94$ is a shape constant. The crystal size *D* was determined for all samples in the previous work[32], but the microstrain was computed here.

The number of liner defects per unit volume of crystal is called dislocation density- η , and it is used to express inversely the crystallinity degree of the nanocrystals. The dislocation density was calculated using the following equation [45]:

$$\eta = \frac{1}{D^2} \tag{4}$$

Furthermore, the probability of a stacking fault is due to the characterization of the crystallization growth process during the crystallization of ZnO nanocrystals [46, 47] and was obtained using the equation:

$$S.F. = \left(2\pi^2/45\sqrt{3}\right)\Delta(2\theta)/\tan \theta. \tag{5}$$

The residual stress in the gigapascal unit was computed using the following equation:

$$Stress = 450\frac{C_o - C}{C_o} \text{ GPa}, \tag{6}$$

For a single-crystalline ZnO, $c_o = 0.5206 \text{ nm}$ [47].

Assuming the spherical shape of ZnO nanoparticles, the number of formed ZnO unit cells per particle [48] was computed by:

$$N = \frac{4\pi\left(\frac{D_x}{2}\right)^3}{3V}, \tag{7}$$

where *V* is the unit cell volume

The probability of porosity *P* of the particles [49], which is related to the aggregation, was determined by the equation:

$$P = \left(1 - \frac{d_{bulk}}{d_x}\right), \tag{8}$$

Where d_{bulk} , d_x are the densities for bulk and X-ray of the prepared ZnO nanoparticles.

In addition, the entire surface area of a particle per unit of its mass is known as a specific surface area (SSA) for a particle and was calculated by the equation[50]:

$$SSA = \frac{6000}{D \times d_{bulk}} \tag{9}$$

It is known that the peaks in the X-ray diffraction patterns represent the sites of crystallization inside the bio-synthesized ZnO samples, and the intensity of these peaks expresses the growth rate of nanocrystals present in these sites or directions [51–53]. It is shown in Table 3 that the sample PZ1(at 25 °C) has the highest intensity at peak position 36.34°, which means that the growth rate was faster at room temperature while the nucleation rate was slower, and this allowed the formation of a small number of small ZnO crystals as shown the number of unit cell per a nanoparticle. Sample PZ4 has the lowest intensity, which indicates a large number of ZnO nanocrystals were formed at peak position 36.39°, and this means the nucleation rate was faster at the same time the growth rate was slower. For that reason, sample PZ4 has larger crystals than sample PZ1. At a suitable temperature, the two processes (nucleation and growth)

Table 3 Peak position(2θ), full width of half maximum(FWHM), intensity(I), average crystal size(D_a), lattice strain(ϵ), dislocation density(η), stacking fault(S.F.), residual stress, prosody(P), and specific surface area(SSA) parameters of the ZnO nanocrystals samples

Temp. ($^{\circ}\text{C}$)	2θ deg	FWHM deg	I a.u	D_a nm	$\epsilon \times 10^{-3}$	$\eta \times 10^{-4}$ (nm) 2	S.F. $\times 10^{-2}$	stress GP	$P \times 10^2$	SSA $\text{m}^2.\text{g}^{-1}$	$N \times 10^3$
25	31.84	0.210	141	35.23	0.338	8.06	0.787	0.519	1.492	30.358	482.26
	34.49	0.185	108				0.759				
	36.34	0.236	235				1.057				
35	31.93	0.174	109	47.77	0.250	4.38	1.474	1.124	1.695	22.389	1204.78
	34.59	0.201	80.3				1.514				
	36.41	0.174	172				1.642				
50	31.83	0.256	125	49.96	0.238	4.01	0.713	0.346	1.359	21.408	1373.49
	34.49	0.174	108				0.673				
	36.32	0.166	212				0.889				
65	31.89	0.212	98.3	48.51	0.246	4.25	1.210	1.470	1.849	22.047	1263.62
	34.58	0.212	80				1.416				
	36.39	0.171	171				1.475				
75	31.95	0.265	91.8	38.88	0.307	6.62	1.569	1.124	1.909	27.508	650.99
	34.60	0.211	91.5				1.582				
	36.44	0.214	178				1.895				
90	31.79	0.223	137	36.79	0.323	7.39	0.491	0.605	1.436	29.071	548.89
	34.46	0.186	117				0.472				
	36.29	0.226	210				0.639				

develop at a relative rate and form large crystal sizes as well as large numbers of unit cells as in sample PZ3. The rest values of intensity and crystal size can be understood using the same concept.

The width of these peaks reflects the extent of deformation inside these ZnO nanocrystals, the narrow peaks indicate high crystallinity, and the wide peaks are due to a high deformation rate in the crystalline structure of the ZnO nanocrystal samples [54]. Here, this deformation was computed with different forms such as microstrain, dislocation density, residual stress, and stacking fault.

The microstrain, dislocation density, and specific surface area parameters depend on the crystal size. Table 3 shows that samples with small crystal sizes have greater microstrain, dislocation density, and specific surface area, which are related to the appropriate temperature for the balance of nucleation and growth processes to form crystal or amorphous ZnO nanoparticles [40]. The prepared ZnO nanocrystals sample at 50 $^{\circ}\text{C}$ (PZ3) has the largest crystal size and the smallest microstrain, dislocation density, and specific surface area.

The stacking fault in the arrangement of the atoms inside the zinc oxide crystal can be verified by observing the shift that occurred in the positions of the X-ray diffraction peaks of the prepared samples and comparing them with the standard JCPDS card No. 80-0075 peaks, especially at the major peak as shown in Table 1 [55]. The previous assumption was that stacking fault decreases with increasing temperature [55], but it appears in this work that this deformation depends on the

rate and direction of ZnO nanocrystal growth [56] as shown in Table 3.

For the explanation of residual stress in ZnO nanocrystals, it is observed from Table-1 that d_{hkl} for the standard is larger than d_{hkl} for the prepared samples. This indicated that the type of residual stresses was tensile stresses on the surface of the ZnO nanocrystals [48]. Actually, this residual stress was due to the traces of the precursor (propolis) in the form of hydroxyl (OH) groups on the surface of the prepared ZnO nanoparticle samples, which was proven in IR spectra in previous work [32]. The existence of these OH groups as defect sites was demonstrated in the emission of the PL spectra in the next section. This residual stress changed nonlinearly with biosynthesis temperature, and this is also evidence of the unbalanced rates of nucleation and growth processes.

The porosity of the prepared ZnO nanoparticle is due to the microstrain in the crystal structure, which is caused by the aggregation of ZnO nanocrystals [57]. The porosity probability is mainly proportional to the residual stress. The OH groups on the surface of ZnO nanocrystals caused surface tensile stress, which contributed to amplifying nanocrystal boundaries and increasing vacancies [58], as exhibited in Table 3.

UV–Vis absorption and optical parameters of ZnO nanoparticles

Figure 3 shows the UV–Vis absorption of the prepared samples of ZnO nanoparticles. The photoactivity of zinc oxide

nanocrystals is determined by a number of factors, including particle accumulation, surface area, porosity, size, synthesis method, and gap energy[59–61]. The differentiated behavior of the prepared samples in the photoactivity is observed, and there is no clear linear relationship between the biosynthesis temperature and the photoactivity.

Sample PZ6 appears to absorb more ultraviolet at the region (200–368 nm) compared to the others, while sample PZ5 has more transmittance than the others in the same wavelength range, as shown in Figs. 3 and 4. In the

wavelength range of 370 nm to 700 nm, the prepared sample at room temperature (PZ1) has the highest transmittance percentage, while the prepared sample at 65 °C (PZ4) has the highest visible absorption.

ZnO nanoparticles’ optical parameters

The UV-Vis absorption spectra analysis revealed different optical properties for the prepared samples of ZnO

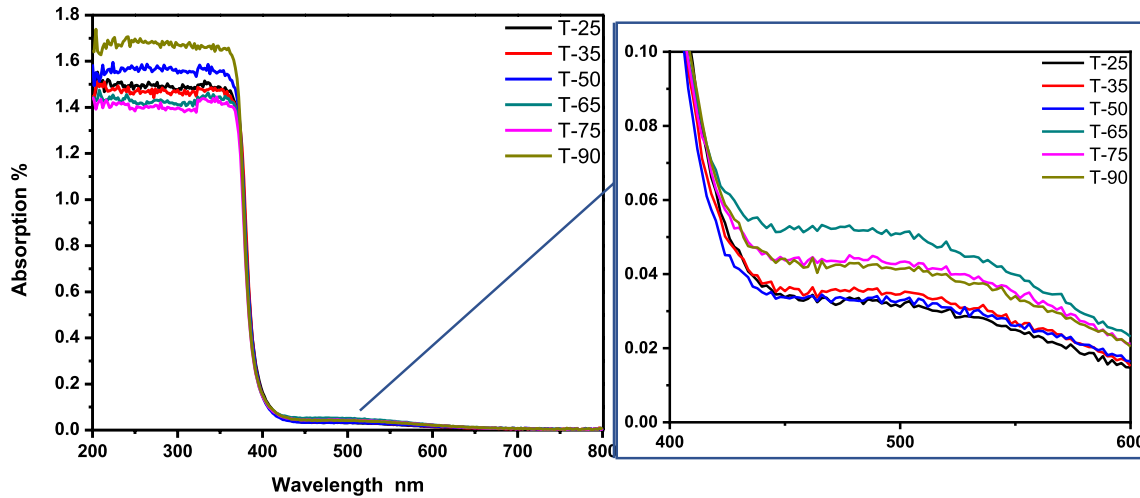


Fig. 3 The UV–Vis absorption of the prepared samples of ZnO nanoparticles

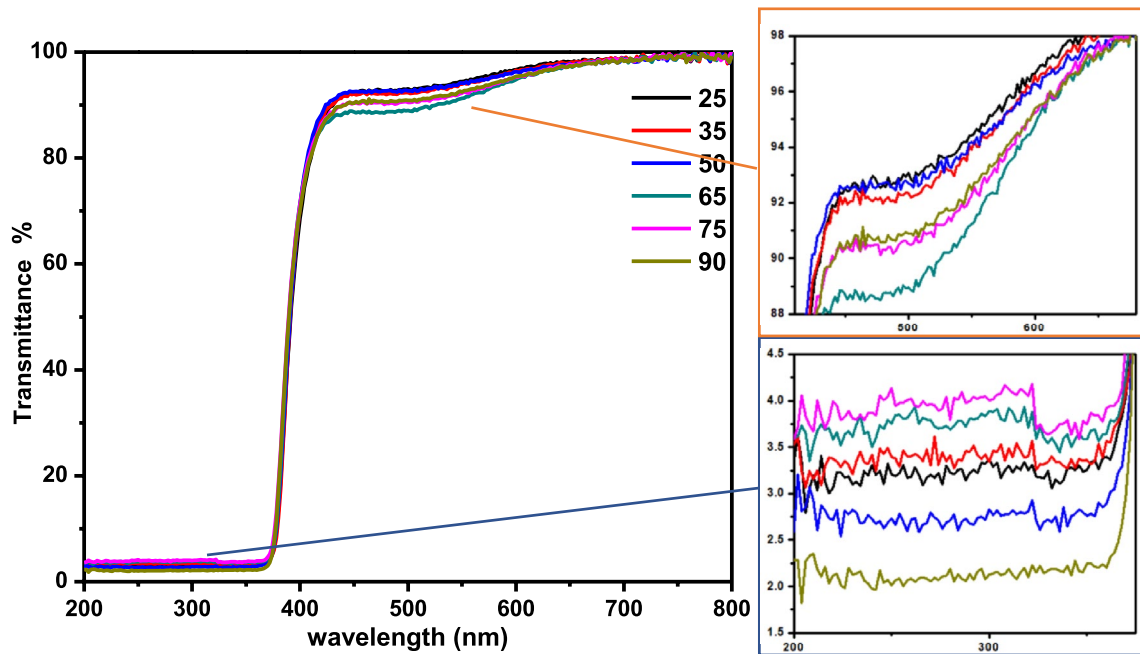


Fig. 4 The UV–Vis transmittance of the prepared samples of ZnO nanoparticles

nanoparticles. In this section, some optical parameters were estimated as follows:

Absorption coefficient, extinction coefficient, and skin depth The intensity attenuation of the light passing through a material is called the absorption coefficient. The total cross section of absorption for an optical process per unit volume of a material can be used to define the absorption coefficient. This attenuation of the light depends on the optical path or the thickness of the sample, and the absorption coefficient was calculated using the following equation [62]:

$$\alpha = \frac{2.303}{s} A, \quad (10)$$

Where A is the UV–Vis absorption and s is the sample's thickness (~ 1 mm).

In Fig. 5a, the absorption coefficient values increase as the biosynthesis temperature rises. Whereas at the sudden absorption edge (3.45 eV), this relationship appeared to be nonlinear, as shown in Fig. 5b, and this may be due to the presence of a difference in the size of the zinc oxide nanocrystals and the formation of energy levels for the crystalline defects [63, 64].

The ability of a material to absorb or reflect at particular wavelengths is represented by its extinction coefficient ϵ , which can be calculated as follows [62]:

$$\epsilon = \frac{\alpha \lambda}{4\pi}, \quad (11)$$

Numerous variables, including the extinction coefficient, material type, conductivity, and thickness of the material in

the absorption band, govern how much energy is absorbed by a material. In Fig. 6, the extinction coefficient values of the prepared samples ranged from 8.8×10^{-6} to 10.3×10^{-6} . The approximate linear fit of the biosynthesis temperature with the extinction coefficient shows a proportional relationship, which means the high extinction coefficient is due to the large particle size and the high absorption coefficient because all the prepared samples have the same concentration [65].

The skin depth of a nanoparticle is the thin shell close to the particle's surface at which radiation and light interaction with the particle is significantly reduced. The skin depth of the synthesized samples was determined using the absorption coefficient, which depends on the incident photon energy and the absorbance percentage. Using the absorption coefficient α , the skin depth δ can be computed as follows:

$$\delta = \frac{1}{\alpha}, \quad (12)$$

Figure 7 shows clearly that the skin depth of the ZnO nanocrystal samples decreases with the increase in the energy of radiation until ~ 3 eV, and then it becomes constant for higher energies. At the UV region, sample PZ5 has the highest penetration depth against the energy of UV radiation, while samples PZ6 and PZ3 show the minimum penetration depth. This means that samples with a high concentration of ZnO nanocrystals and a wide band gap are more resistant to radiation penetration [66].

Energy band gap and Urbach energy According to our earlier research, the band gap energies (E_g) of the biosynthesized ZnO samples were calculated using the cutoff wavelength at which the edge of absorption goes up, as shown in

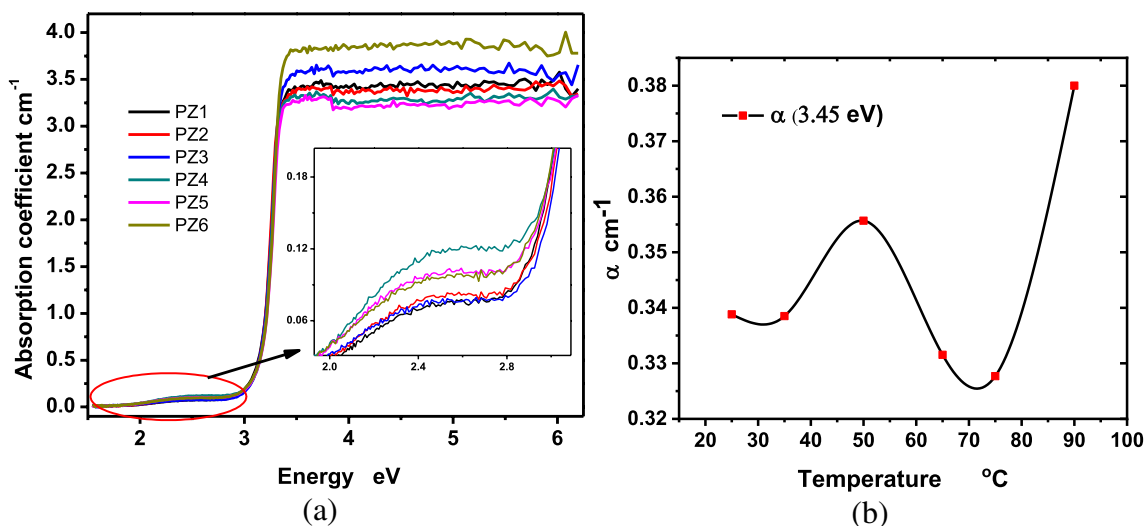


Fig. 5 **a** Absorption coefficient as a function of the energy of radiation. **b** Absorption coefficient as a function of temperature at 3.45 eV for all prepared samples

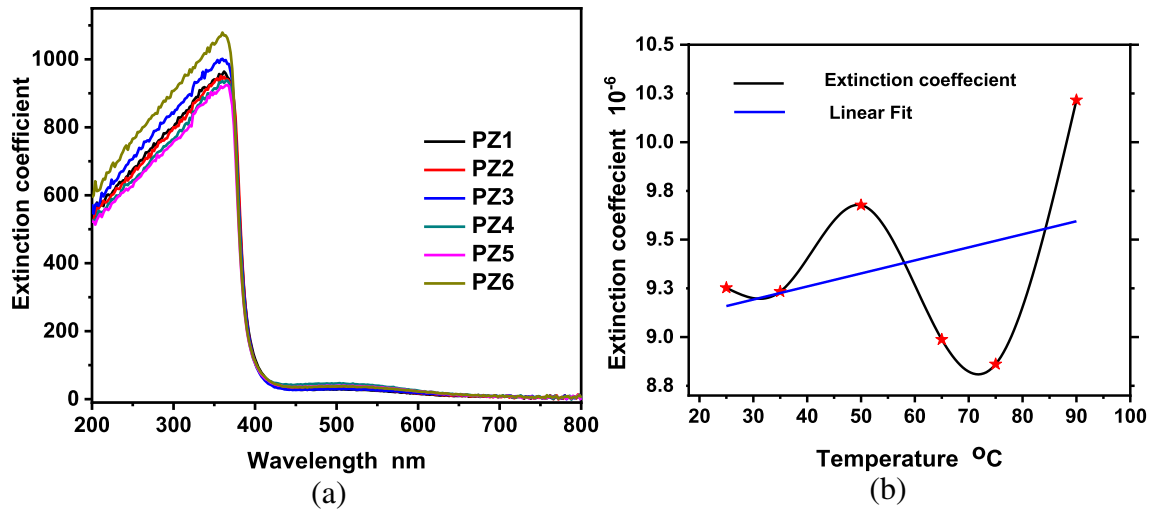


Fig. 6 **a** Extinction coefficient as a function of the wavelength of radiation. **b** Extinction coefficient as a function of temperature at 3.61 eV (~ 343.5 nm) for all prepared samples

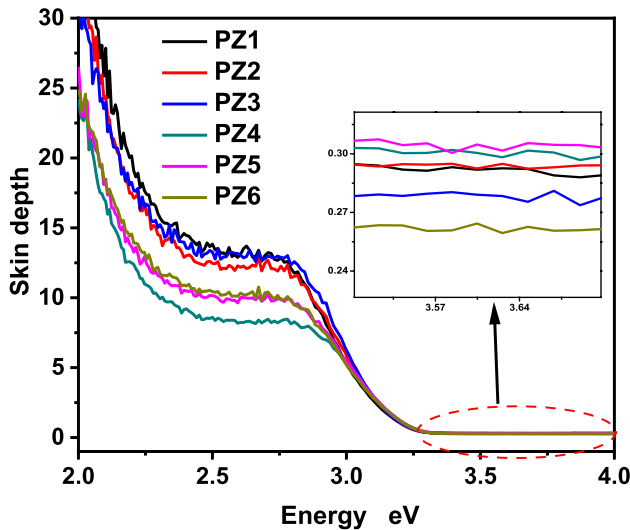


Fig. 7 The skin depth parameter vs. energy of radiation for the prepared ZnO samples

Fig. 3. Table 4 contains the calculated band gap energies for all the prepared samples, which were determined using the following equation [32]:

$$E_g = 1240/\lambda \tag{13}$$

where E_g is the band gap energy in electron volts and λ is the wavelength in nanometers.

For more accuracy, the energy gap was calculated using Tauc’s equation [67]:

$$\alpha h\nu = F(h\nu - E_g)^m \tag{14}$$

where F is a constant, m is a constant but it depends on the energy band structure ($m=0.5$ for direct band gap and $m=2$ for indirect band gap). By plotting the relation between $(\alpha h\nu)^{1/m}$ and $h\nu$, the energy gap was obtained and listed in Table 4. It is known that the band gap of ZnO nanoparticles is 3.37 eV, but our data shows less than this value due to the presence of propolis (flavonoids), which acts as a donor and forms an n-type ZnO semiconductor and in turn reduces the energy gap [68].

The effect of the biosynthesis temperature on the energy gap is shown by the change in the crystal size, as the crystal size decreases with the increase in the biosynthesis temperature, and the decrease in the crystal size is associated with the increase in the energy gap due to the decrease in the overlapping energy orbitals [69, 70].

The density of electronic transition states or the distortion of the nanostructure can be calculated using the Urbach energy value as follows [71]:

$$\ln(\alpha) = \ln(\alpha_0) + h\nu/E_u \tag{15}$$

where α_0 denotes a constant and E_u denotes the Urbach energy. The Urbach energy values for all samples were calculated using the reciprocal of the slope of the relationship $\ln(\alpha)$ and $h\nu$, and these values are listed in Table 4. The Urbach energy increases with increasing biosynthesis temperature, except in the PZ1 sample. This indicates that the rise in biosynthesis temperature enhances the formation of defect states in the energy gap [72]. The sample PZ2 has the lowest Urbach energy value, which suggests less density defect states. These formations of defect states can be

Table 4 Cutoff wavelength, refractive index (using different models), energy gap (using cutoff wavelength and Tauc’s equation), and Urbach energy for the prepared samples

Sample	cutoff wavelength nm	Energy gap eV	n-Moss	n—Rav	n—Herv	n—Red	n—Kum	E _g —dir. Tauc	E _g in average eV	E _U meV
PZ1	393.37	3.152	2.343019	2.129	1.145	2.726	2.325	3.223	3.188	110.58
PZ2	391.08	3.171	2.339601	2.118	1.144	2.722	2.321	3.220	3.196	121.24
PZ3	390.2	3.178	2.338284	2.114	1.144	2.720	2.319	3.232	3.203	110.26
PZ4	389.79	3.181	2.33767	2.112	1.144	2.719	2.319	3.230	3.206	110.36
PZ5	388.99	3.188	2.336469	2.108	1.143	2.718	2.317	3.239	3.213	117.51
PZ6	387.61	3.199	2.334394	2.101	1.143	2.715	2.314	3.243	3.221	118.98

demonstrated using photoluminescence measurements, as will be discussed later.

Refractive index There are many optical and electrical properties of nanomaterials in numerous studies and applications that are related to the refractive index [73]. Despite being difficult to measure the refractive index of nanoparticles, it is regarded as a critical property. Since the refractive index and energy gap are related, the refractive index was determined using five different models as shown in the following equations:

The square root relationship model was given by Moss as [74]:

$$n = \left(\frac{95}{E_g}\right)^{0.25} \tag{16}$$

The liner relationship model was given by Ravindra as [75]:

$$n = 4.084 - 0.62E_g \tag{17}$$

The Ravindra’s model was modified by Herve and Vandamme [76] to be:

$$n = \sqrt{1 + \left(\frac{13.6}{E_g + 3.47}\right)^2} \tag{18}$$

The logarithm relationship model proposed by Dionne and Woolley [77] as follows:

$$n = \left(\frac{154}{E_g - 0.365}\right)^{0.25} \tag{19}$$

The Kumar and Singh model [78] for calculating the refractive index as:

$$n = 3.3668(E_g)^{-0.32234} \tag{20}$$

In Table 4, it is clearly observed that there is an inverse relationship between the temperature of ZnO biosynthesis

and the refractive index (in all models) as well as a proportional relationship with the energy gap. The increase in refractive index is evidence of the formation of energy states of defects in ZnO nanostructure semiconductors, which is accompanied by a decrease in the energy gap, but this depends on the mechanism of ZnO nanocrystals formation [79]. The refractive index for the prepared ZnO nanocrystal samples ranges from 1.14 to 2.72, which is in good agreement with previous work [80].

Optical conductivity The nanoparticles’ reaction with radiation is measured via their optical conductivity property [81]. This optical conductivity parameter is dependent on the wavelength of the incident radiation and is also influenced by the refractive index and absorption coefficient of the nanoparticles. It can be estimated using the following equation [81]:

$$\sigma = \frac{n\alpha v}{4\pi} \tag{21}$$

where v is speed of the electromagnetic radiation. Figure 8 shows the optical conductivity as a function of wavelength.

The sudden increase in the optical conductivity of the ZnO nanocrystals at the beginning of the ultraviolet radiation region is evidence of the intense interaction of these nanocrystals with UV radiation and their absorption [62, 66], but this interaction depends on the size of the nanocrystals and their energy gap. This optical conductivity shows the ability of these nanocrystals to block ultraviolet radiation. From Fig. 8, PZ6 and PZ3 samples have higher optical conductivity ($1.5\text{--}1.8 \times 10^9 \text{ s}^{-1}$) than the others in the UV spectrum, while PZ4 and PZ5 have higher optical conductivity ($3\text{--}6 \times 10^7 \text{ s}^{-1}$) in the visible spectrum.

ZnO nanoparticles’ UV-blocking parameters

One of the most common applications of ZnO nanoparticles in the textile industry is UV radiation protection. The UV-Vis absorption measurements were employed to find out the UV-blocking parameters of

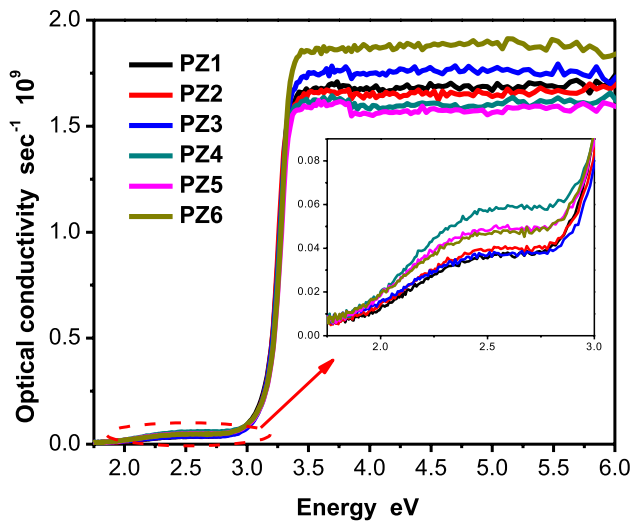


Fig. 8 The optical conductivity vs. radiation energy for all the prepared samples

the biosynthesized ZnO nanoparticle samples in the range of wavelengths 280 nm to 400 nm. In this range of wavelengths, there are two types of UV radiation. The first type is UV-A, which emits radiation in the range of 315 nm to 400 nm, and the second type is UV-B, which emits radiation in the range of 280 nm to 315 nm. The UV-blocking parameters for the prepared samples were calculated using the following equations [82–84]:

$$\text{Ultraviolet transmission percentage UV - A}(T)\% = \frac{\sum_{315}^{400} T(\lambda)}{400 - 315} \quad (22)$$

$$\text{Ultraviolet transmission percentage UV - B}(T)\% = \frac{\sum_{280}^{315} T(\lambda)}{315 - 280} \quad (23)$$

$$\text{Ultraviolet blocking percentage UV - A}(blocking)\% = 100 - T_{UV-A} \quad (24)$$

$$\text{Ultraviolet blocking percentage UV - B}(blocking)\% = 100 - T_{UV-B} \quad (25)$$

Table 5 UV-transmission % and UV-blocking parameters of the biosynthesis ZnO nanoparticles samples

Temp	B(290–315)		A(315–400)	
	UV-transmission %	UV-blocking	UV-transmission %	UV-blocking
25	16.45	69.45	11.24	78.05
35	15.65	70.94	10.95	78.62
50	19.50	63.79	12.93	74.74
65	14.04	73.94	10.15	80.17
75	13.26	75.38	9.61	81.23
90	25.26	53.10	16.02	68.71

The $T(\lambda)$, T_{UV-A} , and T_{UV-B} are the spectral transmission of the samples, and the average transmittance in the corresponding spectral regions (A & B), respectively.

It is observed from Table 5 that the prepared sample at 75 °C has the highest blocking percentage. This percentage of blocking increases in wavelength region A (315–400) nm.

As confirmed in the previous parameters, the ultraviolet ray blocking property of ZnO nanocrystals depends strictly on their nanostructure and optical properties in terms such as their size, crystal shape, surface area, and energy levels of impurities present in the energy gap. Therefore, the increase in the biosynthesis temperature during the preparation of these ZnO nanocrystals samples led to the overlap of these parameters and factors, which in turn also led to the absence of a clear linear relationship between this property, UV-blocking, and the biosynthesis temperature on the other hand [85–88].

Photoluminescence-PL analysis

The presence of impurities within the zinc oxide nanoparticles is verified by photoluminescence intensity measurements. These impurities were formed due to the biosynthesis of these nanoparticles using propolis. The photoluminescence spectra of the prepared samples are shown in Fig. 9a. The PL spectra for the samples revealed that the strong peaks are in the range of (399.85–403.2 nm), which agreed with the reported work [89, 90]. The peaks of the strong PL spectra intensity of all the prepared samples shifted to a short wavelength except for the prepared sample at 50 °C, which shifted to a long wavelength. As shown in Fig. 9b, there is a nonlinear relationship between the PL spectra intensity and the biosynthesis temperature of the ZnO samples. The highest PL intensity was for the prepared sample at 35 °C, while the lowest was for the prepared sample at 50 °C.

The higher PL intensity indicates the denser intrinsic defects due to the calcination process, which was conducted after the growth of ZnO nanocrystals [91]. The lower the PL intensity, the slower the recombination emission, which means effective photocatalysis [91, 92]. The peaks positions in the photoluminescence spectrum are typically related to band-to-defect level or band-to-band

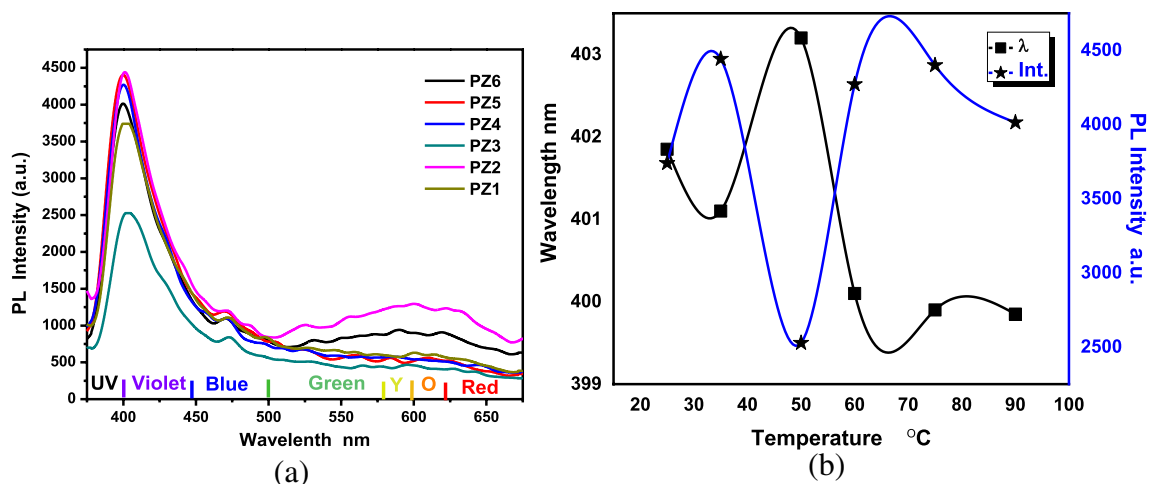


Fig. 9 **a** The photoluminescence spectra of all the prepared samples. **b** The peaks' positions and intensities in the strong PL spectra for all the prepared samples

transitions, or with the recombination of excitons (electron-hole pairs). In Figure 9-a, the peak position redshift [93, 94] of the strong PL emission for the prepared sample PZ3 indicates that this sample is the largest particle size, as proved by XRD results. The full-width-half-maximum of the PL spectra can be used to describe the biosynthesis time for nanocrystal growth, excited state density, as well as the symmetry or asymmetry in the shape, size, and defects [95–99]. In Fig. 10, a deconvolution was performed using a compiled function (Gaussian) for the PL spectra of all the prepared samples using PEAKFIT software. The identification and removal of the curves' baselines were performed. It is clear from Fig. 10a that most of the samples have sharp peaks with high intensities in the ultraviolet and violet regions. Small peaks of intensity are shown in the blue region for all the prepared samples. Furthermore, only the two samples prepared at 35 and 90 °C also have higher broad peaks in regions extending from the green to the red region. Table 6 shows the peaks resulting from the deconvolution of PL spectra for all the prepared samples. Table 6 demonstrated the excited states within the formed ZnO nanocrystals.

The ultraviolet emission in PL spectra (200–400 nm) is attributed to excitons' states (free and bound) and phonons' interactions and is explained by the deformation potential that occurred in ZnO nanocrystals [100, 101]. This excitons state has highest density in the sample PZ4, which is observed from the intensity of PL spectra in Table-6.

The violet emission in PL spectra (400–450 nm) is due to two types of defects, interstitial zinc- Zn_i and Zinc atom vacancy- V_{Zn} [102, 103]. The green synthesis of ZnO nanocrystals using propolis extract enhanced the relaxation of zinc atoms, and this allowed two hydrogen–oxygen bonds to be generated on the surface of ZnO nanocrystals. This

process is called the source of zinc interstitials [104]. The transition from the conduction band to the state of zinc atom vacancy (V_{Zn}) called a “deep hole trapped level” [105]. These defects have higher density in all samples.

The blue emission (450–490 nm) in PL spectra is caused by the transition from oxygen atoms interstitials (O_i ~2.69 eV), some vacancies of zinc atoms (V_{zn} ~2.66 eV), and extended Zn_i states (~2.59 eV) to the valance band. According to the defect ionization reaction, these extended states can be created during the heating treatment [101–106]. This type of defect has highest density in the sample PZ2.

For the green emission (490–570 nm) in PL spectra, the oxygen vacancy (V_O ~2.22 eV) and oxygen antisite vacancy O_{Zn} defects were assumed to be formed during the calcination of the sample [105, 107, 108]. As well as the transitions from conduction band to oxygen atom interstitial (O_i ~2.28 eV) located above the valance band were responsible for the green emission. This defect is responsible to form acceptor states in nanosemiconductor [106]. These defects are noted clearly in samples PZ2 and PZ6. These types of defects (excitons-phonon, V_O , and Zn_i) are responsible to form donor states in ZnO nanosemiconductor.

The yellow-orange emissions in PL spectra are deep band emissions caused by the transitions from conduction band or Zn_i states to O_i states (~2.06 to 2.17 eV). The O_i states are located above the valance band and responsible to form acceptor states in nanosemiconductor [101, 106]. These defects are existence densely in PZ2 and PZ6.

The red emission in PL spectra is assigned to be two steps transitions. The first step is from conduction band to V_O or O_i states, which are situated near the center of the band gap. The second step is from V_O or O_i states to valance band (~2 to 1.7 eV) [106]. These defects increased in the samples PZ2 and PZ6.

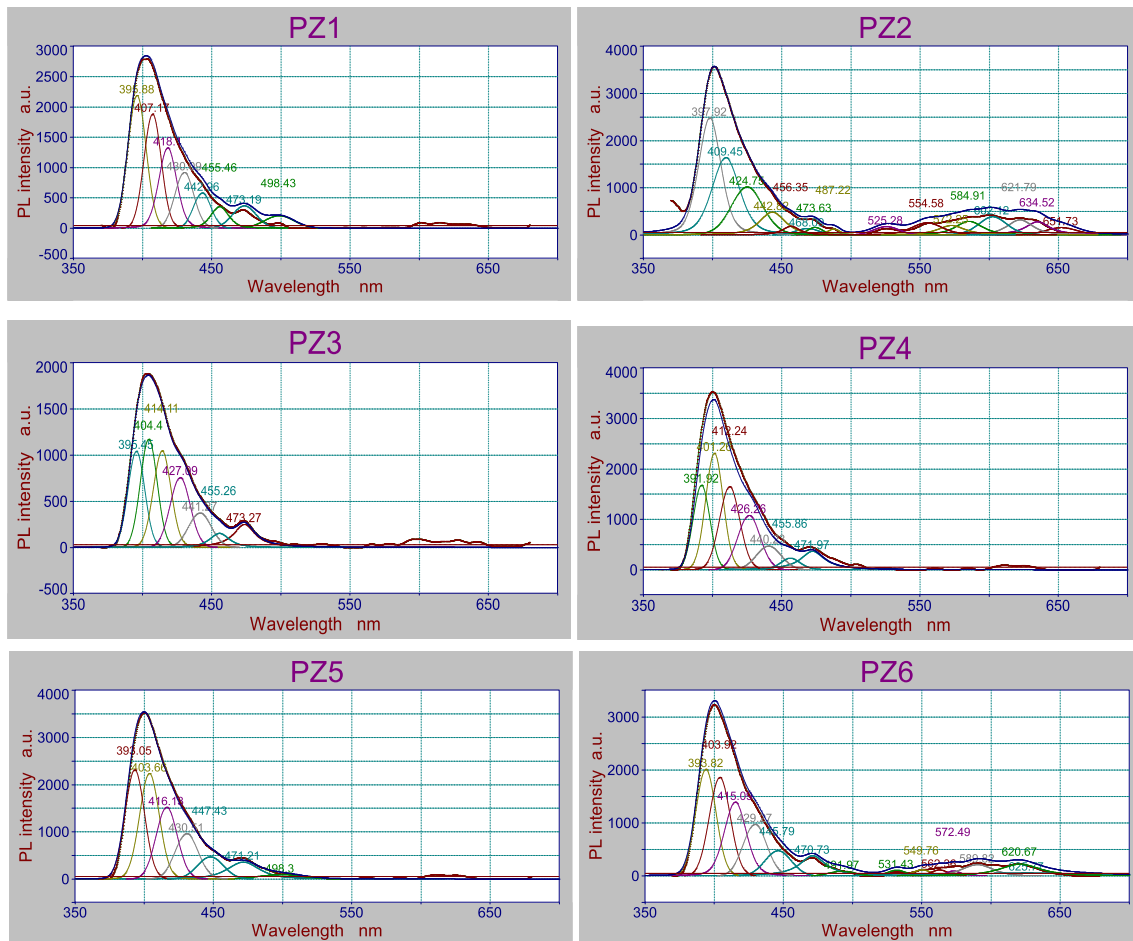


Fig. 10 The deconvoluted PL spectra for all prepared samples

The fluctuating effect of the biosynthesis temperature during the formation of zinc oxide nanocrystals may be explained based on two hypotheses as follows: The first is that with the increase in the biosynthesis temperature, a time difference occurs between the nucleation and growth processes, which causes this difference in the sizes of the zinc oxide nanocrystals, and in turn, on the structure and properties. While the second hypothesis is based on the fact that with the increase in the biosynthesis temperature, the collisions that hinder the nucleation and growth processes increase in a way that leads to a difference in the sizes of the zinc oxide nanocrystals [109].

TEM analysis

Most of the findings in this work depend on the XRD results to confirm the size and shape of these nanoparticles, TEM micrograph was taken for ZnO nanoparticles that biosynthesized at 50°C. Figure 11 illustrates how zinc oxide nanoparticles are imaged via TEM, which reveals their sizes and shapes. Additionally, it appears that these

particles possess a polygonal shape. It can be noted that some particles have a hexagonal shape., which coincides with the crystal structure of zinc oxide. Their sizes range from 13.921 to 102.97 nm with an average of 43.42 nm, which is approximately similar to the results of crystal size from X-ray diffraction patterns.

Conclusion

The research conclusions can be summarized as follows: The results of this research showed that the hypothesis of increasing the reaction temperature (during the formation of zinc oxide nanoparticles) in biosynthesis using propolis does not affect the optical properties as well as the crystalline structure parameters of these nanoparticles in a linear way, as was thought.

A large number of microstructure parameters, optical properties, and UV-blocking parameters were computed

Table 6 The intensities, peak positions, full-width-half-maximum, and energies of deconvoluted PL spectra for all the prepared samples

Peak	PZ1					PZ2					PZ3				
	Intensity (a.u.)	Wavelength nm	FWHM nm	Energy eV		Intensity (a.u.)	Wavelength nm	FWHM nm	Energy eV		Intensity (a.u.)	Wavelength nm	FWHM nm	Energy eV	
1	2189.6	395.88	15.51	3.132	2484.9	397.92	19.08	3.116	1042.7	395.45	14.22	3.136			
2	1883.8	407.18	14.63	3.045	1640.4	409.46	23.58	3.028	1173.2	404.41	14.34	3.066			
3	1326.7	418.10	15.16	2.966	1020.2	424.75	26.71	2.919	1046.9	414.11	15.03	2.994			
4	921.8	430.09	16.01	2.883	485.9	442.82	21.75	2.800	757.2	427.09	17.10	2.903			
5	582.1	442.96	14.84	2.799	183.7	456.35	14.83	2.717	374.3	441.27	19.23	2.810			
6	356.2	455.46	15.11	2.723	136.1	468.09	19.73	2.649	152.9	455.26	16.89	2.724			
7	369.6	473.19	20.15	2.621	159.1	473.63	13.09	2.618	250.3	473.28	18.70	2.620			
8	206.2	498.43	22.81	2.488	124.5	487.22	10.37	2.545							
9					176.9	525.28	21.75	2.361							
10					259.3	554.58	26.36	2.236							
11					200.3	572.25	23.30	2.167							
12					290.3	584.91	22.79	2.120							
13					386.1	602.12	23.79	2.059							
14					321.5	621.79	21.72	1.994							
15					280.2	634.53	20.98	1.954							
16					155.6	651.73	26.72	1.903							
PZ4	PZ5														
Peak	Intensity (a.u.)	Wavelength nm	FWHM nm	Energy eV	Intensity (a.u.)	Wavelength nm	FWHM nm	Energy eV	Intensity (a.u.)	Wavelength nm	FWHM nm	Energy eV			
1	1678.3	391.92	14.21	3.164	2315.8	393.05	16.49	3.155	2013.8	393.82	17.09	3.149			
2	2313.7	401.26	14.91	3.090	2378.2	403.69	16.71	3.072	1859.6	403.92	17.80	3.070			
3	1650.5	412.24	17.15	3.008	1654.9	416.15	17.96	2.980	1395.7	415.09	18.65	2.987			
4	1078.7	426.26	19.04	2.909	1163.3	430.58	19.53	2.880	975.3	429.27	20.11	2.889			
5	470.8	440.23	21.07	2.817	608.6	447.81	21.99	2.769	477.3	445.79	22.36	2.782			
6	231.0	455.86	16.71	2.720	601.7	470.89	27.07	2.633	384.7	470.73	22.52	2.634			
7	366.5	471.97	20.99	2.627	310.6	498.28	37.01	2.489	111.2	531.43	16.04	2.333			
8					296.8	532.26	21.89	2.330	118.9	549.76	15.18	2.256			
9									115.5	562.36	14.73	2.205			
10									214.7	589.82	26.73	2.102			
11									224.7	620.67	35.22	1.998			

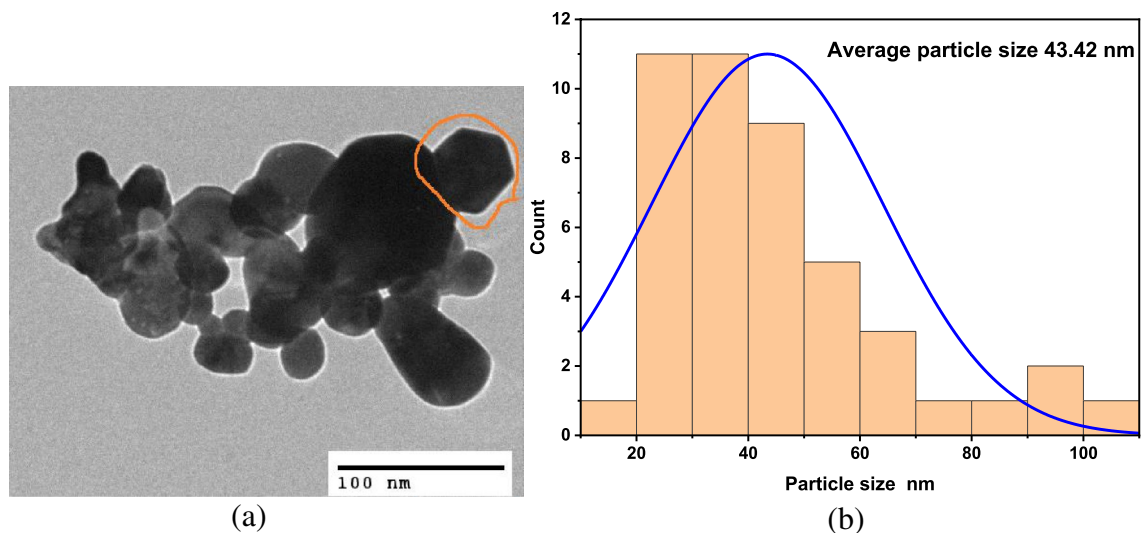


Fig. 11 **a** Micrograph of ZnO nanoparticles and **b** the size distribution of ZnO nanoparticles

with high accuracy using experimental results and reported international studies.

The outcomes of this work showed the possibility of controlling these properties through temperature and biosynthesis using bee products (propolis).

The results also confirmed that the use of propolis enhanced the properties of zinc oxide nanoparticles through the formation of ZnO n-type nano-semiconductors, reduced the energy gap, and increased the energy states of defects formed, which increased the UV absorption by these ZnO nanocrystals and reduced their dangers.

It was discovered that the biosynthesis temperature of ZnO nanoparticles has a nonlinear effect on their structural and optical properties as well as UV-blocking parameters. The direct cause of this nonlinear relationship was the discrepancy between the speeds of nucleation and growth rates for ZnO nanoparticles.

Author contributions The authors confirm contribution to the paper as follows: MA and SOMO helped in study conception and design; SOMO and MSAG helped in data collection; MA, SOMO, MSAG, and MAA helped in analysis and interpretation of results; SOMO, MSAG, MSA, and AMQ helped in draft manuscript preparation. All authors reviewed the results and approved the final version of the manuscript.

Data and code availability The authors declare that the data supporting the findings of this study are available within the paper.

Declarations

Conflict of interest The authors declare that they have no known competing financial interests or personal relationships that could have appeared to influence the work reported in this paper.

Ethical approval Not Applicable.

References

1. B. Dibley, B. Neilson, Climate crisis and the actuarial imaginary: the war on global warming. *New Form* **69**(69), 144–159 (2010)
2. E. Kavalski, From the cold war to global warming: observing complexity in IR. *Polit. Stud. Rev.* **9**(1), 1–12 (2011)
3. H. Mohamed, M. Elayah, and L. Schuplen, Yemen between the impact of the climate change and the ongoing Saudi-Yemen war: a real tragedy, *Cent. Int. Dev. Issues*, Nijmegen, Netherlands, (2017)
4. A. Noaman, G. Petersen, J. Kiesel, S. Wade, Climate change impacts on water resources in Yemen. *J. Earth Sci. Eng.* **3**(9), 629 (2013)
5. J. Hostager, Fleeing from a forgotten war: refugees in the context of the conflict in Yemen. *J. Int. Relations* **20**, 21–41 (2018)
6. Yemen Six Month Economic Analysis Economic Warfare & the Humanitarian Context, (2017). [Online]. Available: <https://sr-indonesia.com/wp-content/uploads/2017/04/IARAN-YEMEN-6-month-analysis-REPORT-1.pdf>
7. A. Ibrahim, K. El Rhazi, B. Benazzouz, and S. Mohammed, Knowledge and Public Awareness of Cancer Risk Factors and Determinants among Yemeni adults-A Community Based Cross-Sectional Study, in *E3S Web of Conferences*, EDP Sciences, (2021), 1051. <https://doi.org/10.1051/e3sconf/202131901051>
8. I.A. Ba-Saddik, Childhood cancer in Aden, Yemen. *Cancer Epidemiol* **37**(6), 803–806 (2013)
9. A. Bin AlZou, M.A. Bin Thabit, K.A. AlSakkaf, H.O. Basaleem, Skin cancer: clinicopathological study of 204 patients in Southern Governorates of Yemen. *Asian Pac. J. Cancer Prev.* **17**(7), 3195–3199 (2016)

10. R.B. Weller, The health benefits of UV radiation exposure through vitamin D production or non-vitamin D pathways. Blood pressure and cardiovascular disease. *Photochem. Photobiol. Sci.* **16**(3), 374–380 (2017)
11. S. Malinović-Miličević, Z. Mijatović, G. Stanojević, M.M. Radovanović, V. Popović, Health risks of extended exposure to low-level UV radiation—an analysis of ground-based and satellite-derived data. *Sci. Total Environ.* **831**, 154899 (2022)
12. Q.-B. Chen et al., Platinum (IV) complex-loaded nanoparticles with photosensitive activity for cancer therapy. *Coord. Chem. Rev.* **472**, 214789 (2022)
13. R. Narain, *Polymer Science and Nanotechnology: Fundamentals and Applications*. Elsevier, (2020)
14. E.B. Souto et al., Nanomaterials for skin delivery of cosmetics and pharmaceuticals. *Appl. Sci.* **10**(5), 1594 (2020)
15. B. Bulcha et al., Synthesis of zinc oxide nanoparticles by hydrothermal methods and spectroscopic investigation of ultraviolet radiation protective properties. *J. Nanomater.* **2021**, 1–10 (2021)
16. I.A. Channa, J. Ashfaq, S.J. Gilani, A.A. Shah, A.D. Chandio, M. N. bin Jumah, UV blocking and oxygen barrier coatings based on polyvinyl alcohol and zinc oxide nanoparticles for packaging applications. *Coatings* **12**(7), 897 (2022)
17. S.P.K. Malhotra, T. Mandal, Zinc oxide nanostructure and its application as agricultural and industrial material. *Contam. Agric. Environ. Heal. Risks Remediat.* **1**, 216 (2019)
18. A. Rawat, U. Soni, R.S. Malik, S.C. Pandey, Facile synthesis of UV blocking nano-sized zinc oxide and polymethylmethacrylate polymer nanocomposite coating material. *NanoStruct. Nano-Objects* **16**, 371–380 (2018)
19. M. Parashar, V.K. Shukla, R. Singh, Metal oxides nanoparticles via sol–gel method: a review on synthesis, characterization and applications. *J. Mater. Sci. Mater. Electron.* **31**(5), 3729–3749 (2020)
20. G.K. Dalapati et al., Tin oxide for optoelectronic, photovoltaic and energy storage devices: a review. *J. Mater. Chem. A* **9**(31), 16621–16684 (2021)
21. P.A. Luque et al., Facile zinc oxide nanoparticle green synthesis using citrus reticulata extract for use in optoelectronic sensors. *IEEE Sens. J.* **21**(10), 11275–11282 (2020)
22. N. Cole et al., Topical ‘Sydney’ propolis protects against UV-radiation-induced inflammation, lipid peroxidation and immune suppression in mouse skin. *Int. Arch. Allergy Immunol.* **152**(2), 87–97 (2010)
23. M.V. Butnariu, C.V. Giuchici, The use of some nanoemulsions based on aqueous propolis and lycopene extract in the skin’s protective mechanisms against UVA radiation. *J. Nanobiotechnol.* **9**(1), 1–9 (2011)
24. Y. Fu et al., Propolis inspired sunscreens for efficient UV-protection and skin barrier maintenance. *Nano Res.* **15**(9), 8237–8246 (2022)
25. U. Manzoor, F.T. Zahra, S. Rafique, M.T. Moin, M. Mujahid, Effect of synthesis temperature, nucleation time, and post-synthesis heat treatment of ZnO nanoparticles and its sensing properties. *J. Nanomater.* **16**(1), 9–9 (2015). <https://doi.org/10.1155/2015/189058>
26. C. M. Pelicano, E. Magdaluyo, and A. Ishizumi, Temperature dependence of structural and optical properties of ZnO nanoparticles formed by simple precipitation method, in *MATEC Web of Conferences*, EDP Sciences, (2016), p 2001
27. P. Muniraja, K. Sunil Kumar, M. Ramanadha, A. Sudharani, M. Ravi, R.P. Vijayalakshmi, Effect of synthesis temperature on structural, optical, and magnetic properties of ZnO nanoparticles synthesized by combustion method. *J. Supercond. Nov. Magn.* **32**, 2175–2183 (2019)
28. A.K. Zak, M.E. Abrishami, W.H.A. Majid, R. Yousefi, S.M. Hosseini, Effects of annealing temperature on some structural and optical properties of ZnO nanoparticles prepared by a modified sol–gel combustion method. *Ceram. Int.* **37**(1), 393–398 (2011)
29. M.R. Parra, F.Z. Haque, Aqueous chemical route synthesis and the effect of calcination temperature on the structural and optical properties of ZnO nanoparticles. *J. Mater. Res. Technol.* **3**(4), 363–369 (2014)
30. W.L. de Almeida, N.S. Ferreira, F.S. Rodembusch, V.C. de Sousa, Study of structural and optical properties of ZnO nanoparticles synthesized by an eco-friendly tapioca-assisted route. *Mater. Chem. Phys.* **258**, 123926 (2021)
31. R. Amari et al., Ni doping effect on the electronic, structural and optical properties of ZnO nanoparticles prepared by Coprecipitation route. *Opt. Mater.* **128**, 112398 (2022)
32. M.S. Osman, M. Al-qubati, M. Saeed, N. Abdulqawi, M.A. Algradee, A. Alwan, A.M. Sultan, Effective inhibition of waterborne and fungal pathogens using ZnO nanoparticles prepared from an aqueous extract of propolis: optimum biosynthesis, characterization, and antimicrobial activity. *Appl. Nanosci.* **13**(6), 4515–4526 (2022)
33. S.O. Mohamed, K. El-Naggar, M.M.H. Khalil, Green synthesis of silver nanoparticles using egyptian propolis extract and its antimicrobial activity. *Egypt. J. Chem.* **65**(7), 5–6 (2022)
34. R. Chen, K.A. Jakes, D.W. Foreman, Peak-fitting analysis of cotton fiber powder X-ray diffraction spectra. *J. Appl. Polym. Sci.* **93**(5), 2019–2024 (2004)
35. S.O.A. Asbahi, R.M. Kershi, The X-ray diffraction microstructure analysis of hexagonal ferrite powders doped with La rare earth ions. *J. Chem. Crystallogr.* **42**, 155–158 (2012)
36. V. Koutu, L. Shastri, M.M. Malik, Effect of NaOH concentration on optical properties of zinc oxide nanoparticles. *Mater. Sci.* **34**(4), 819–827 (2016)
37. Ö.A. Yıldırım, H.E. Unalan, C. Durucan, Highly efficient room temperature synthesis of silver-doped zinc oxide (ZnO: Ag) nanoparticles: structural, optical, and photocatalytic properties. *J. Am. Ceram. Soc.* **96**(3), 766–773 (2013)
38. V.P. Deshpande, S.D. Sartale, A.N. Vyas, A.U. Ubale, Temperature dependent properties of spray deposited nanostructured ZnO thin films. *Int. J. Mater. Chem.* **7**(2), 36–46 (2017)
39. A. Belay, B. Bekele, A.R.C. Reddy, Effects of temperature and polyvinyl alcohol concentrations in the synthesis of zinc oxide nanoparticles. *Dig. J. Nanomater. Biostruct.* **14**(1), 51–60 (2019)
40. H. Liu, H. Zhang, J. Wang, J. Wei, Effect of temperature on the size of biosynthesized silver nanoparticle: deep insight into microscopic kinetics analysis. *Arab. J. Chem.* **13**(1), 1011–1019 (2020)
41. E.Y. Shaba, J.O. Jacob, J.O. Tijani, M.A.T. Suleiman, A critical review of synthesis parameters affecting the properties of zinc oxide nanoparticle and its application in wastewater treatment. *Appl. Water Sci.* **11**, 1–41 (2021)
42. N.T.K. Thanh, N. Maclean, S. Mahiddine, Mechanisms of nucleation and growth of nanoparticles in solution. *Chem. Rev.* **114**(15), 7610–7630 (2014)
43. J.D. Zwilling et al., Understanding lignin micro- and nanoparticle nucleation and growth in aqueous suspensions by solvent fractionation. *Green Chem.* **23**(2), 1001–1012 (2021)
44. A.K. Zak, W.H.A. Majid, M.E. Abrishami, R. Yousefi, X-ray analysis of ZnO nanoparticles by Williamson-Hall and size-strain plot methods. *Solid State Sci.* **13**(1), 251–256 (2011)
45. S. Mustapha et al., Comparative study of crystallite size using Williamson-Hall and Debye-Scherrer plots for ZnO nanoparticles. *Adv. Nat. Sci. Nanosci. Nanotechnol.* **10**(4), 45013 (2019)

46. M.-C. Jeong, S.-W. Lee, J.-M. Seo, J.-M. Myoung, The effect of stacking fault formation on optical properties in vertically aligned ZnO nanowires. *Nanotechnology* **18**(30), 305701 (2007)
47. M. Kahouli, A. Barhoumi, A. Bouzid, A. Al-Hajry, S. Guermazi, Structural and optical properties of ZnO nanoparticles prepared by direct precipitation method. *Superlatt. Microstruct.* **85**, 7–23 (2015)
48. K. Lingaraju et al., Biogenic synthesis of zinc oxide nanoparticles using *Ruta graveolens* (L.) and their antibacterial and antioxidant activities. *Appl. Nanosci.* **6**, 703–710 (2016)
49. Y.T. Prabhu, K.V. Rao, V.S.S. Kumar, B.S. Kumari, Synthesis of ZnO nanoparticles by a novel surfactant assisted amine combustion method. *Adv. Nanoparticles* **2**(01), 45 (2013)
50. A. Sahai, N. Goswami, Structural and vibrational properties of ZnO nanoparticles synthesized by the chemical precipitation method. *Phys. E Low-dimensional Syst. Nanostruct.* **58**, 130–137 (2014)
51. G.S. Thool, A.K. Singh, R.S. Singh, A. Gupta, M.A.B.H. Susan, Facile synthesis of flat crystal ZnO thin films by solution growth method: a micro-structural investigation. *J. Saudi Chem. Soc.* **18**(5), 712–721 (2014)
52. H. Wasly, X-ray analysis for determination the crystallite size and lattice strain in zno nanoparticles. *J. Al-Azhar Univ. Eng. Sect.* **13**(49), 1312–1320 (2018)
53. D. Tahir and K. H. Jae, Effect of growth temperature on structural and electronic properties of ZnO thin films, in *AIP Conference Proceedings*, AIP Publishing LLC, (2017), p 20007
54. R. Yogamalar, R. Srinivasan, A. Vinu, K. Ariga, A.C. Bose, X-ray peak broadening analysis in ZnO nanoparticles. *Solid State Commun.* **149**(43–44), 1919–1923 (2009)
55. T. Mahalingam, V.S. John, L.S. Hsu, Microstructural analysis of electrodeposited zinc oxide thin films. *J. New Mater. Electrochem. Syst.* **10**(1), 9 (2007)
56. X. Wang, Q. Li, Z. Liu, J. Zhang, Z. Liu, R. Wang, Low-temperature growth and properties of ZnO nanowires. *Appl. Phys. Lett.* **84**(24), 4941–4943 (2004)
57. C.T. Quy, C.M. Hung, N. Van Duy, N.D. Hoa, M. Jiao, H. Nguyen, Ethanol-sensing characteristics of nanostructured ZnO: nanorods, nanowires, and porous nanoparticles. *J. Electron. Mater.* **46**, 3406–3411 (2017)
58. S.K. De et al., Zone-specific crystallization and a porosity-directed scaling marker for the catalytic efficacy of Au–Ag alloy nanoparticles. *ACS Appl. Nano Mater.* **2**(12), 7669–7685 (2019)
59. R. Rhodes, M. Horie, H. Chen, Z. Wang, M.L. Turner, B.R. Saunders, Aggregation of zinc oxide nanoparticles: from non-aqueous dispersions to composites used as photoactive layers in hybrid solar cells. *J. Colloid Interface Sci.* **344**(2), 261–271 (2010)
60. M.C. Uribe-López et al., Photocatalytic activity of ZnO nanoparticles and the role of the synthesis method on their physical and chemical properties. *J. Photochem. Photobiol. A Chem.* **404**, 112866 (2021)
61. H. Sudrajat, S. Babel, Ultrahigh photoactivity of ZnO nanoparticles for decomposition of high-concentration microcystin-LR in water environment. *Int. J. Environ. Sci. Technol.* **16**, 695–706 (2019)
62. A. Sangeetha, S. Jaya Seeli, K.P. Bhuvana, M.A. Kader, S.K. Nayak, Correlation between calcination temperature and optical parameter of zinc oxide (ZnO) nanoparticles. *J. Sol–Gel Sci. Technol.* **91**, 261–272 (2019)
63. A.H. Moharram, S.A. Mansour, M.A. Hussein, M. Rashad, Direct precipitation and characterization of ZnO nanoparticles. *J. Nanomater.* **2014**, 20 (2014)
64. M.G. Kotresh, M.K. Patil, S.R. Inamdar, Reaction temperature based synthesis of ZnO nanoparticles using co-precipitation method: Detailed structural and optical characterization. *Optik (Stuttg)* **243**, 167506 (2021)
65. D. Segets, J. Gradl, R.K. Taylor, V. Vassilev, W. Peukert, Analysis of optical absorbance spectra for the determination of ZnO nanoparticle size distribution, solubility, and surface energy. *ACS Nano* **3**(7), 1703–1710 (2009)
66. R. Sagheer, S.T. Khadija, Z.N. Kayani, S. Riaz, Structural, optical and magnetic properties of ZnO nanoparticles tailored by ‘La3+’ ions. *Optik (Stuttg)* **244**, 166816 (2021)
67. L. Ma et al., Improved photocatalytic activity via N-type ZnO/p-type NiO heterojunctions. *Nanomaterials* **12**(20), 3665 (2022)
68. H. Çolak, E. Karaköse, Green synthesis and characterization of nanostructured ZnO thin films using *Citrus aurantifolia* (lemon) peel extract by spin-coating method. *J. Alloys Compd.* **690**, 658–662 (2017)
69. D. Suresh, P.C. Nethravathi, H. Rajanaika, H. Nagabhushana, S.C. Sharma, Green synthesis of multifunctional zinc oxide (ZnO) nanoparticles using *Cassia fistula* plant extract and their photodegradative, antioxidant and antibacterial activities. *Mater. Sci. Semicond. Process.* **31**, 446–454 (2015)
70. N. Kamarulzaman, M.F. Kasim, R. Rusdi, Band gap narrowing and widening of ZnO nanostructures and doped materials. *Nanoscale Res. Lett.* **10**, 1–12 (2015)
71. K.J. Archana, A.C. Preetha, K. Balasubramanian, Influence of Urbach energy in enhanced photocatalytic activity of Cu doped ZnO nanoparticles. *Opt. Mater. (Amst)* **127**, 112245 (2022)
72. K. Omri, I. Najeh, R. Dhahri, J. El Ghoul, L. El Mir, Effects of temperature on the optical and electrical properties of ZnO nanoparticles synthesized by sol–gel method. *Microelectron. Eng.* **128**, 53–58 (2014)
73. F. Iskandar, Nanoparticle processing for optical applications—a review. *Adv. Powder Technol.* **20**(4), 283–292 (2009)
74. T.S. Moss, A relationship between the refractive index and the infra-red threshold of sensitivity for photoconductors. *Proc. Phys. Soc. Sect. B* **63**(3), 167 (1950)
75. N.M. Ravindra, S. Auluck, V.K. Srivastava, On the Penn gap in semiconductors. *Phys. status solidi* **93**(2), K155–K160 (1979)
76. P. Herve, L.K.J. Vandamme, General relation between refractive index and energy gap in semiconductors. *Infrared Phys. Technol.* **35**(4), 609–615 (1994)
77. G. Dionne, J.C. Woolley, Optical properties of some Pb 1–x Sn x Te alloys determined from infrared plasma reflectivity measurements. *Phys. Rev. B* **6**(10), 3898 (1972)
78. V. Kumar, J.K. Singh, Model for calculating the refractive index of different materials. *Indian J. Pure Appl. Phys.* **48**, 571–574 (2010)
79. O.G. Abdullah, S.B. Aziz, K.M. Omer, Y.M. Salih, Reducing the optical band gap of polyvinyl alcohol (PVA) based nanocomposite. *J. Mater. Sci. Mater. Electron.* **26**, 5303–5309 (2015)
80. S.D. Senol, B. Yalcin, E. Ozugurlu, L. Arda, Structure, microstructure, optical and photocatalytic properties of Mn-doped ZnO nanoparticles. *Mater. Res. Express* **7**(1), 15079 (2020)
81. M. Ghanipour, D. Dorrani, Effect of Ag-nanoparticles doped in polyvinyl alcohol on the structural and optical properties of PVA films. *J. Nanomater.* **2013**, 2 (2013)
82. T.R. Kar, A.K. Samanta, M. Sajid, R. Kaware, UV protection and antimicrobial finish on cotton khadi fabric using a mixture of nanoparticles of zinc oxide and poly-hydroxy-amino methyl silicone. *Text. Res. J.* **89**(11), 2260–2278 (2019)
83. S. Dadvar, H. Tavanai, M. Morshed, UV-protection properties of electrospun polyacrylonitrile nanofibrous mats embedded with MgO and Al 2 O 3 nanoparticles. *J. Nanoparticle Res.* **13**, 5163–5169 (2011)

84. Y. Li, Y. Zou, Y. Hou, Fabrication and UV-blocking property of nano-ZnO assembled cotton fibers via a two-step hydrothermal method. *Cellulose* **18**, 1643–1649 (2011)
85. Z. Mao, Q. Shi, L. Zhang, H. Cao, The formation and UV-blocking property of needle-shaped ZnO nanorod on cotton fabric. *Thin Solid Films* **517**(8), 2681–2686 (2009)
86. Y.M. Im, T.H. Oh, J.A. Nathanael, S.S. Jang, Effect of ZnO nanoparticles morphology on UV blocking of poly (vinyl alcohol)/ZnO composite nanofibers. *Mater. Lett.* **147**, 20–24 (2015)
87. X. Wang, X. Sun, X. Guan, Y. Wang, X. Chen, X. Liu, Tannic interfacial linkage within ZnO-loaded fabrics for durable UV-blocking applications. *Appl. Surf. Sci.* **568**, 150960 (2021)
88. V. Gupta, R. Jain, V.K. Sharma, A. Srivastava, L. Kumar, Investigation of UV blocking properties of ZnO/PMMA free-standing flexible sheets. *Mater. Today Proc.* **62**, 7308–7313 (2022)
89. Z. Wang, H. Zhang, L. Zhang, J. Yuan, S. Yan, C. Wang, Low-temperature synthesis of ZnO nanoparticles by solid-state pyrolytic reaction. *Nanotechnology* **14**(1), 11 (2002)
90. D. Raoufi, Synthesis and photoluminescence characterization of ZnO nanoparticles. *J. Lumin.* **134**, 213–219 (2013)
91. A. N. Kadam, J. Lee, S. V Nipane, and S.-W. Lee, Nanocomposites for visible light photocatalysis, in *Nanostructured Materials for Visible Light Photocatalysis*, Elsevier, (2022), p 295–317.
92. J. G. R. Sereni, Reference module in materials science and materials engineering, (2016)
93. P.H. Krishna, M. Ramrakhiani, Nano particle size effect on photo-luminescence. *Int. J. Nanotechnol. Appl.* **4**(1), 13–19 (2010)
94. V. Kravets et al., Imaging of biological cells using luminescent silver nanoparticles. *Nanoscale Res. Lett.* **11**(1), 1–9 (2016)
95. R. K. Willardson, E. R. Weber, and M. Sugawara, *Self-Assembled InGaAs/GaAs Quantum Dots*. Academic Press, (1999)
96. B.S. Rao, B.R. Kumar, V.R. Reddy, T.S. Rao, G. Chalapathi, Preparation and characterization of CdS nanoparticles by chemical co-precipitation technique. *Chalcogenide Lett.* **8**(3), 177–185 (2011)
97. K. S. & A. P. Vira Kravets, Zamavang Almemar, Ke Jiang, Kyle Culhane, Rosa Machado, Guy Hagen, Andriy Kotko, Igor Dmytruk, Narrow emission from Rb3Sb2I9 nanoparticles, *Adv. Opt. Mater.*, **8**(1): 1901606, (2020)
98. P. Zhou, X. Zhang, L. Li, X. Liu, L. Yuan, X. Zhang, Temperature-dependent photoluminescence properties of Mn: ZnCuInS nanocrystals. *Opt. Mater. Express* **5**(9), 2069–2080 (2015)
99. D.W. Hamby, D.A. Lucca, M.J. Klopstein, G. Cantwell, Temperature dependent exciton photoluminescence of bulk ZnO. *J. Appl. Phys.* **93**(6), 3214–3217 (2003)
100. C. Chandrinou, N. Boukos, C. Stogios, A. Travlos, PL study of oxygen defect formation in ZnO nanorods. *Microelectronics J.* **40**(2), 296–298 (2009)
101. H. Zeng, G. Duan, Y. Li, S. Yang, X. Xu, W. Cai, Blue luminescence of ZnO nanoparticles based on non-equilibrium processes: defect origins and emission controls. *Adv. Funct. Mater.* **20**(4), 561–572 (2010)
102. S. Ben Ameer et al., Enhanced photocatalytic activity against crystal violet dye of Co and In doped ZnO thin films grown on PEI flexible substrate under UV and sunlight irradiations. *Helvion* **5**(6), e01912 (2019)
103. P.K. Upadhyay, N. Sharma, S. Sharma, R. Sharma, Photo and thermoluminescence of Eu doped ZnO nanophosphors. *J. Mater. Sci. Mater. Electron.* **32**(13), 17080–17093 (2021)
104. M. Ali, M. Winterer, ZnO nanocrystals: surprisingly ‘alive.’ *Chem. Mater.* **22**(1), 85–91 (2010)
105. T.K. Kundu, N. Karak, P. Barik, S. Saha, Optical properties of ZnO nanoparticles prepared by chemical method using poly (vinyl alcohol)(PVA) as capping agent. *Int. J. Soft Comput. Eng.* **1**, 19–24 (2011)
106. A. Galdámez-Martínez, G. Santana, F. Güell, P.R. Martínez-Alanis, A. Dutt, Photoluminescence of ZnO nanowires: a review. *Nanomaterials* **10**(5), 857 (2020)
107. M. Zhang, F. Averseng, J.-M. Krafft, P. Borghetti, G. Costentin, S. Stankic, Controlled formation of native defects in ultrapure ZnO for the assignment of green emissions to oxygen vacancies. *J. Phys. Chem. C* **124**(23), 12696–12704 (2020)
108. J. Wang, R. Chen, L. Xiang, S. Komarneni, Synthesis, properties and applications of ZnO nanomaterials with oxygen vacancies: a review. *Ceram. Int.* **44**(7), 7357–7377 (2018)
109. K. Karthick, P. Kathirvel, R. Marnadu, S. Chakravarty, M. Shkir, Ultrafast one step direct injection flame synthesis of zinc oxide nanoparticles and fabrication of p-Si/n-ZnO photodiode and characterization. *Phys. B Condens. Matter* **612**, 412971 (2021)

Publisher’s Note Springer Nature remains neutral with regard to jurisdictional claims in published maps and institutional affiliations.

Springer Nature or its licensor (e.g. a society or other partner) holds exclusive rights to this article under a publishing agreement with the author(s) or other rightsholder(s); author self-archiving of the accepted manuscript version of this article is solely governed by the terms of such publishing agreement and applicable law.